Journal of Marine Research, 59, 725–747, 2001

Geostrophy via potential vorticity inversion in the Yucatan Channel

by J. Ochoa[1], J. Sheinbaum[1], A. Badan[1], J. Candela[1] and D. Wilson[2]

ABSTRACT

It has become common practice to measure ocean current velocities together with the hydrography by lowering an ADCP on typical CTD casts. The velocities and densities thus observed are considered to consist mostly of a background contribution in geostrophic balance, plus internal waves and tides. A method to infer the geostrophic component by inverting the linearized potential vorticity (P_V) provides plausible geostrophic density and velocity distributions. The method extracts the geostrophic balance closest to the measurements by minimizing the energy involved in the difference, supposed to consist of P_V-free anomalies. The boundary conditions and the retention of P_V by the geostrophic estimates follow directly from the optimization, which is based on simple linear dynamics and avoids both the use of the thermal wind equation on the measured density, and the classical problem of a reference velocity. By construction, the transport in geostrophic balance equals the measured one. Tides are the largest source of error in the calculation.

The method is applied to six ADCP/CTD surveys made across the Yucatan Channel in the springs of 1997 and 1998 and in the winter of 1998–1999. Although the time interval between sections is sometimes close to one inertial period, large variations on the order of 10 percent are found from one section to the next. Transports range from 20 to 31 Sv with a net average close to 25 Sv, consisting of 33 Sv of inflow into the Gulf of Mexico and 8 Sv of outflow into the Caribbean Sea. The highest velocities are 2.0 m sec^{-1} into the Gulf of Mexico near the surface on the western side of the channel, decreasing to 0.1 m sec^{-1} by 400 to 500 m depth. Beneath the core of the Yucatan Current a countercurrent, with speeds close to 0.2 m sec^{-1} and an average transport of 2 Sv, hugs the slopes of the channel from 500 to 1500 m depth. Our data show an additional 6 Sv of return flow within the same depth range over the abrupt slope near Cuba, which is likely to be the recirculating fraction of the Yucatan Current deep extention, unable to outflow through the Florida Straits. The most significant southerly flows do not occur in the deepest portion of the channel, but at depths around 1000 m.

1. Introduction

The communication between the Gulf of Mexico and the Caribbean Sea is known as the Yucatan Channel or Straits of Yucatan, though dynamically it is neither a channel, since it is not long enough for its width, nor a strait, since it cannot be considered narrow when compared with the internal Rossby radius of deformation. Nonetheless, it is a confined

1. Oceanografía Física, CICESE, Apdo. Postal 2732, Ensenada, Mexico. ***email: jochoa@cicese.mx***
2. NOAA/AOML, 4301 Rickenbacker Causeway, Miami, Florida, 33149, U.S.A.

section through which flows a major branch of the Subtropical Gyre of the North Atlantic. Almost all of the inflow into the Gulf of Mexico occurs through this region since the inflows in the Florida Straits are small and episodic (Brooks and Niiler, 1977; Lee and Mayer, 1977). We refer to inflows and outflows from the perspective of the Gulf of Mexico.

Direct current measurements in the region date back to Pillsbury (1890) who reported intense currents on the western side of the straits reaching to 200 m depth, with speeds of 1.7 m sec^{-1} at 6.3 m below the surface, and southerly flows on the eastern side of the channel. The western currents were shown to be quite permanent and strong, conforming the Yucatan Current, whose extension feeds the Loop Current of the Gulf of Mexico (Molinari, 1976; Sturges and Evans, 1983). Earlier transport estimates by Schlitz (1973) range from 23 to 33 Sv. The southward current on the eastern side is referred to as the Cuban Countercurrent, first analyzed by Emilsson (1971) and Sukhovey *et al.* (1980). Beneath the Yucatan Current, a southward Yucatan Undercurrent has been shown to play an important role in the upwelling onto the broad Campeche Bank (Merino, 1997). Coastal tidal elevations are small, but tidal currents are not (Durham, 1972; Maul *et al.,* 1985; Carrillo *et al.,* 2000) and will be shown to be the most significant source of errors in our transport estimates.

Classical geostrophic estimates of the flow via hydrographic measurements and the vertical integration of the thermal-wind equation are usually referenced to the deepest common data pairs (Schlitz, 1973; Hansen and Molinari, 1979; Maul *et al.,* 1985; Gallegos *et al.,* 1998), or to a deep reference level (Gordon, 1967), whence deep geostrophic estimates are sluggish at best. Direct measurements by Maul *et al.* (1985) 145 m above the sill show that weekly averages of the currents vary from a maximum southward flow of 10 cm sec^{-1} to a maximum northward flow of 6 cm sec^{-1}, with a net average of 5 cm sec^{-1} to the south. This suggests that deep reference levels might be acceptable for classical geostrophic estimates, since they reproduce the very high speeds where Pillsbury's (1890) and other measurements since have shown them to exist. But, as we will show, there is no definite level of 'no motion' in the Yucatan Channel, and classical geostrophic calculations may be unwarranted, especially for the deeper flows.

The analysis of LADCP/CTD data has renewed discussion on the subject of geostrophically-balanced fields. On the one hand the problem of a reference velocity becomes very different, and on the other we can take into account that the measured hydrography is not necessarily in geostrophic balance. This study shows that the LADCP/CTD data provide direct estimates of the linearized potential vorticity, a field the reader shall recognize as the dynamically natural choice to estimate geostrophy by inversion (see the seminal paper by Hoskins *et al.* (1985) for a review of the subject of P_V inversion). Our inversion method only requires the calculation of the linearized potential vorticity from observations, and its solution provides a single field of geostrophic pressure, of which the geostrophic velocity and geostrophic density are partial derivatives. To carry out the inversion it is necessary to determine the boundary conditions, a task solved by Dikiy (1969) for rectangular

boundaries and whose generalization to irregular boundaries makes the geostrophic estimate possible in practice (disposing of the need for the thermal wind equation and the reference velocity). The conservation of potential vorticity and the boundary conditions are derived from an optimization criteria that seeks geostrophic velocity and density fields which are 'closer' to the measurements or observed fields. As it turns out, the geostrophic estimate fulfills the thermal wind balance by definition, this being a simple matter of the equality of second degree partial derivatives taken in different order.

This study analyzes LADCP/CTD data gathered during six crossings of the Yucatan Channel in the springs of 1997 and 1998 and the winter of 1998–99 in the Yucatan channel, to illustrate the potential vorticity inversion method to infer geostrophy and compare it to the traditional method. We show there exists a possible geostrophic state which is very close to our observations. The following section presents the measurements and their maps across the channel, constructed by objective interpolation. The third section formulates the geostrophic estimation procedure, an optimization principle in the measured velocity as well as in measured density, whose mathematical details are left for an Appendix. We also discuss the sources of error of our calculation, especially the impact of assuming data are simultaneous, when in reality they cannot be. The fourth section compares the results of the inversion to 'classical' estimates obtained via the thermal wind equation, setting their reference velocity with the LADCP by requiring the observed and calculated profiles to have the same vertical integral, as in Beal and Bryden (1999). Transport estimates are also discussed. The fifth section contains discussion and conclusions.

2. Data and vertical maps

Numerous hydrographic casts were taken in the region of the Straits of Yucatan from 23 May to 12 June, 1997, 29 March to 6 May, 1998, and 27 January to 6 February, 1999. The observations were done by lowering a Sea Bird SBE911plus CTD, together with a 300 kHz RD Instruments Acoustic Doppler Current Profiler (ADCP); the package is usually referred to as LADCP, for Lowered ADCP. Figure 1 shows the location of the stations for the first section and typical of all the crossings. Whilst the CTD returns the data in standard fashion through the hydrographic wire, the LADCP stores the data internally, to be read on deck during the transit between stations (Wilson, 1994; Fratantoni and Johns, 1996). Figure 2 shows distributions of velocity and hydrographic properties which are the results from objective-mapping the data of the first crossing onto a grid with spacings of 1 km in the horizontal by 15 m in the vertical. The section was completed in 36 hours, starting from the western side of the channel on 25 May, 1997. Table 1 lists the number of casts, dates and duration of each crossing.

The estimates of partial derivatives were all computed with central differences on the objective maps of the original fields. An objective mapping might use two free parameters to determine the correlation matrix. The first one defines the fraction of the variance increase due to noise, with a unit value representing the signal variance; the second

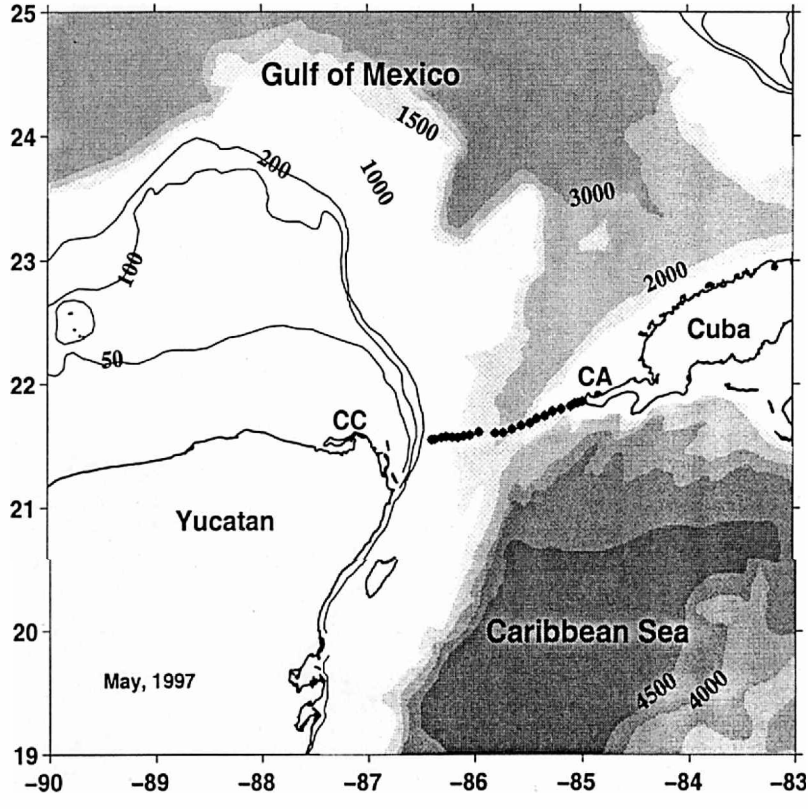

Figure 1. Nominal location of stations, 15 in total, during the first crossing from Cabo Catoche (CC) to Cabo San Antonio (CA), with northern latitude in the abscissas and western longitude in the ordinates. The section channels all the possible exchanges between the Caribbean Sea and the Gulf of Mexico. All other crossings discussed in this study were made along the same section. Isobaths are in meters.

parameter defines the decaying e-folding spatial scale of the correlation (i.e., the distance at which the correlation falls to e^{-1} of its initial value). The correlation function can be exponential or, as used here, Gaussian, but many other correlation functions are possible (explicit examples are shown by Chereskin and Trunnell, 1996). In a physical situation like the one pertaining to this data where the vertical and horizontal length scales differ considerably, a third free parameter defines the aspect ratio or, equivalently, the horizontal and vertical scales can be specified individually. We use a five parameter objective mapping, as described in Roemmich (1983), in which one pair of length scales, 80 m in the vertical and 16.5 km in the horizontal, describes the 'small' scale variability and another pair, 800 m and 165 km, describe the 'large' scale, or background, variability. A fifth parameter, equal to 0.1, describes the noise variances for both scales. (This ratio may be too optimistic for deep velocity observations, which are $O(10\ \mathrm{cm\ sec}^{-1})$ or less, when

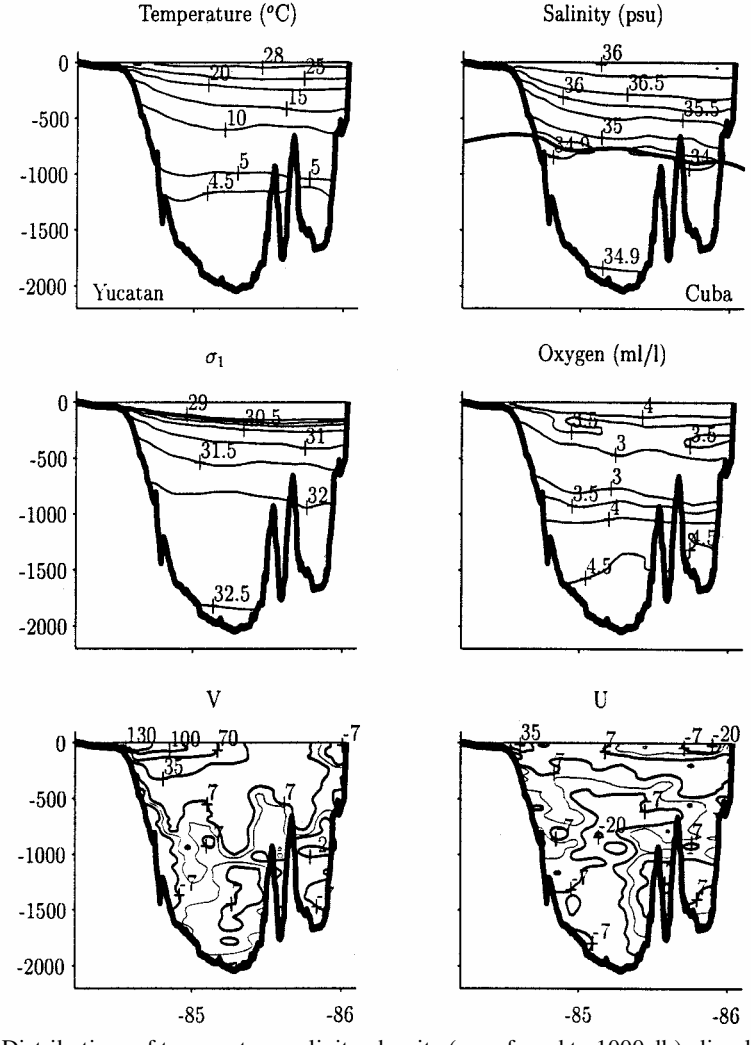

Figure 2. Distributions of temperature, salinity, density (σ_θ referred to 1000 db), dissolved oxygen and the horizontal velocity components (V parallel and U perpendicular to the channel) along the section shown in Figure 1. The axes show depth in meters in the abscissas and western longitude in the ordinates.

LADCP measurement errors are $O(4\ \text{cm sec}^{-1})$.) The Rossby radii of deformation are 44, 25, 15, and 13 km for the first four baroclinic modes, computed with respect to the sill depth (2040 m). Therefore, only the first two modes are somehow retained and the rest are effectively damped. The arithmetic mean and linear trend have been removed prior to the objective mapping, although the effect is unimportant for the parameters used and the data at hand.

Table 1. Information of the six independent crossings made of the Yucatan Channel.

Cruise	Number of profiles	Year	Time at mid-section	Hours to cross
1.a	15	1997	May 26, 11:15	36
1.b	9	1997	May 28, 07:49	25
2.a	13	1998	March 30, 17:11	30
2.b	22	1998	April 4, 20:57	47
3.a	13	1999	Jan 31, 21:42	38
3.b	11	1999	Feb 2, 22:48	47

Well known and typical aspects of the fields are clear in Figure 2. For example, the most intense flows occur near the surface on the western side of the channel; the salinity minimum characteristic of the Antarctic Intermediate Water (AIW) occurs along the $\sigma_1 = 31.938$ (Reid, 1994), the isopycnal shown over the salinity distribution, and the oxygen minimum above the salinity minimum indicates the boundary between the North Atlantic Central Water (NACW) and the Antarctic Intermediate Water (AAIW). Less clear perhaps is the relative oxygen maximum below the subtropical underwater, characteristic of the 18-degree water of North Atlantic origin, which can be seen more easily on the eastern side of the channel. Figure 3 shows the six maps of the velocity into the vertical section, corresponding to each of the crossings listed in Table 1. All show the surface-intensified core of the Yucatan Current, close to the Yucatan shelf break. Most (except 2.a and 2.b) show a surface current flowing into the Caribbean near Cuba. The Yucatan countercurrent and other southerly flows are present beneath the intense surface flows. Of these, the return flow on the deep eastern end of the Yucatan Channel can reach speeds over 30 cm sec^{-1} and is, to our knowledge, observed here for the first time.

3. Geostrophic estimation

The relatively recent development of lowering a package consisting of a CTD and an ADCP measuring simultaneously during hydrographic casts has increased substantially the information gathered during an oceanographic expedition, without requiring much additional shiptime. The studies of Wilson and Leetmaa (1988) and Wilson and Johns (1997) are good examples of the observations that can be gathered in this fashion and of the important information that can be derived from them. Total horizontal velocities can also be obtained with either accurate positioning of the ship (Wilson, 1994) or by using the capability of the ADCP to determine its own motion when the bottom is within its signal range (Fratantoni and Johns, 1996). Techniques to process ADCP data collected in this way have been developed by Fischer and Visbeck (1993) and Wilson (1994); software can be obtained at www.ldeo.columbia.edu/~visbeck/ladcp.

Although the instantaneous velocities across an ocean section give us a direct measure of the transports involved, a valid and important inquiry consists of extracting the semipermanent, or 'balanced,' components of the flow and hydrography by separating them from high-frequency transients, in the hopes that they represent an important fraction whose

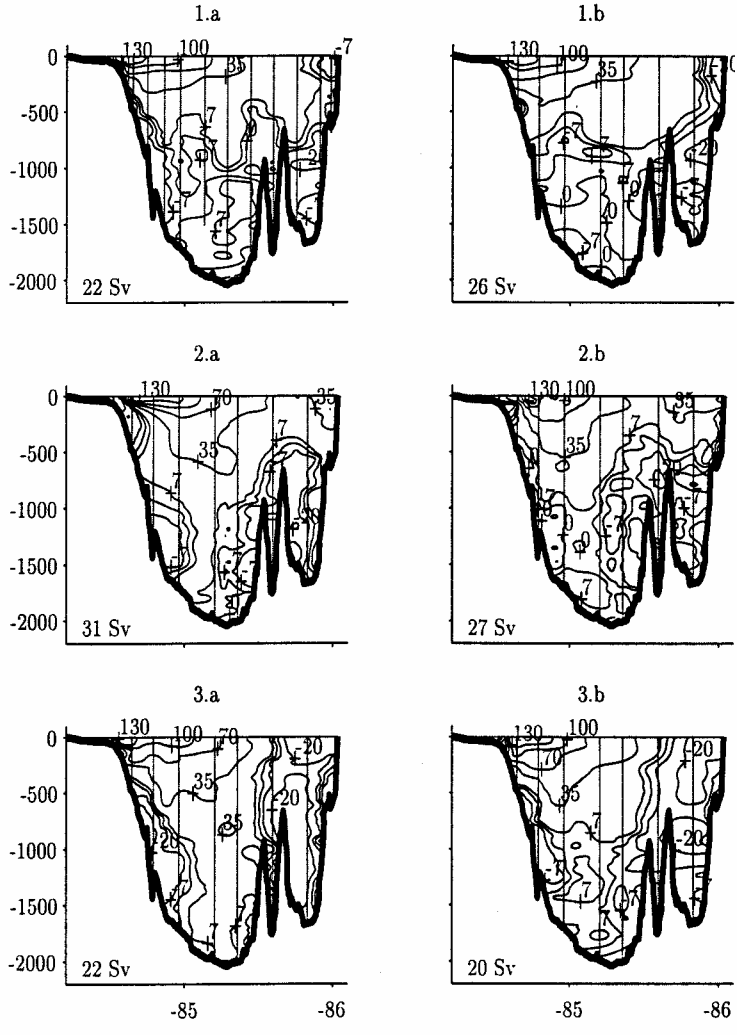

Figure 3. Objective maps of the velocity component perpendicular to the section for each crossing. The dots indicate the data points included in the mapping.

evolution can be best predicted by numerical models. This separation is known as the initialization problem of numerical forecastings, which remains a very modern endeavor of which a huge publication list can be compiled (Daley, 1991). It is also related to the so-called P_V 'invertibility principle' (Hoskins *et al.,* 1985) and to the development of balanced models from first principles. Another reason to determine the geostrophic fields with high precision is to infer upwelling and downwelling motions in frontal zones (Hoskins *et al.,* 1978; Pollard and Regier, 1992; Pinot *et al.,* 1996; Rudnick, 1996), where internal waves are again high-frequency reversible motions that greatly contaminate the

net transport signal. Of course, a portion of the semipermanent contributions might not necessarily be in geostrophic balance; for example, Hinrichsen and Lehman (1995) used such CTD/LADCP profiling measurements to observe significant ageostrophic shears.

Straightforward attempts to use a reference near-surface velocity measured with a ship-mounted ADCP, at a depth where it is hoped that the influence of nongeostrophic processes is small, and then integrate the thermal wind equation on hydrographic data available at depth were made by Saunders (1992) and by Cokelet *et al.* (1996). These methods combine hydrographic observations made in the entire water column with shipboard ADCP velocity measurements in only the top 200–300 m of the ocean. When LADCP data are available in addition to hydrography, the possibilities to estimate geostrophy increase, a straightforward use of which might be as in Beal and Bryden (1999), where baroclinic velocities inferred from the hydrography are matched in the mean with the LADCP current data, with the possible exclusion of the 200 m near the surface where the overlap between observed and geostrophic current shears was less than satisfactory.

A common restriction set in geostrophic velocity estimates based on shipboard ADCP measurements is enforcing nondivergence. This is usually done by finding a streamfunction that reproduces the measured vorticity (as in Pollard and Regier, 1992; Chereskin and Trunnell, 1996), a practice that occurs even with numerical simulations (Pinot *et al.,* 1996). We share the goal of determining the absolute geostrophic velocity in the water column, but the problem is approached with a more general perspective. To have vertical profiles of velocity for the same water columns for which hydrography is available provides the extra advantage that potential vorticity can be computed. The method proposed here goes one step further from previous studies, by adding vertical structure and constructing a pressure function (i.e. geostrophic pressure) that reproduces the measured potential vorticity. But curiously enough, this conservation law is insufficient by itself when derived from the equations of motion because it fails to specify the boundary conditions. We show that a variational (optimization) method (Dikiy, 1969) helps determine those crucial boundary conditions.

a. Analytical formulation

Observed horizontal velocity and hydrography are assumed to consist of the superposition of a geostrophic background, plus ageostrophic and measurement noise contributions. The observed fields are $u = u(\mathbf{r}, t_o)$, $v = v(\mathbf{r}, t_o)$ and $\rho = \rho(\mathbf{r}, t_o)$, where u and v are the zonal and meridional velocity components, ρ is mass density, $\mathbf{r} = (x, y, z)$ is the position with cartesian coordinates x to the east, y to the north, and z upward, and t_o is a time in the middle of data collection. The separation in those contributions can be specified by

$$(\rho_o f v,\ -\rho_o f u,\ -g\rho) = \nabla\tilde{p} + (\rho_o f v',\ -\rho_o f u',\ -g\rho'), \tag{1}$$

where the field $\tilde{p}$ is the geostrophic pressure, the prime denotes ageostrophic plus noise components, f is the Coriolis parameter, ρ_o is a constant mean density, and g is the

gravitational acceleration. It is not, in general, expected that the measurements themselves should fulfill the requirements for the vector $(\rho_o fv, -\rho_o fu, -g\rho)$ to have a potential function (i.e., a plausible function $\tilde{p}$ such that Eq. (1) holds with $u' = v' = \rho' = 0$), since for this to be possible the flow has to be nondivergent and the thermal wind equation must hold for both horizontal components of velocity.

The balance in which the ageostrophic contributions consist of internal waves on the *f*-plane satisfies:

$$u_t - fv = -p_x/\rho_o, \tag{2a}$$

$$v_t + fu = -p_y/\rho_o, \tag{2b}$$

$$w_t = -p_z/\rho_o - \rho g/\rho_o, \tag{2c}$$

$$u_x + v_y + w_z = 0, \tag{2d}$$

$$\rho_t = \rho_o N^2 w/g. \tag{2e}$$

Subscripts denote partial derivatives and ρ is now the anomaly of density with respect to a motionless, horizontally uniform background with density $\bar{\rho} = \bar{\rho}(z)$ that defines the buoyancy frequency squared, $N^2 = -g\bar{\rho}_z/\rho_o$. These do imply

$$\partial_t V_P = \partial_t[v_x - u_y - gf(\rho/N^2)_z/\rho_o] = 0, \tag{3a}$$

a linear invariant which forces all ageostrophic contributions to be P_V-free and, therefore

$$\tilde{v}_x - \tilde{u}_y - gf(\tilde{\rho}/N^2)_z/\rho_o = v_x - u_y - gf(\rho/N^2)_z/\rho_o \tag{3b}$$

at all times, since $v'_x - u'_y - gf(\rho/N^2)_z/\rho_o = 0$, without u', v' and ρ' being at all null. Now, since $\tilde{p}$ defines $\tilde{u}$, $\tilde{v}$ and $\tilde{\rho}$ through

$$-f\tilde{v} = -\tilde{p}_x/\rho_o, \tag{4a}$$

$$f\tilde{u} = -\tilde{p}_y/\rho_o, \tag{4b}$$

$$0 = -\tilde{p}_z - \tilde{\rho}/\rho_o, \tag{4c}$$

(see Eq. 1) Eq. (3b) reads simply

$$\tilde{p}_{xx} + \tilde{p}_{yy} + f^2\left(\frac{\tilde{p}_z}{N^2}\right)_z = \rho_o f(v_x - u_y) - gf^2\left(\frac{\rho}{N^2}\right)_z. \tag{3c}$$

In short, accepting that the dominant contribution to ageostrophy comes from internal waves, the solution to Eq. (3c), whose left side is provided by the measurements, produces the geostrophic contribution. In Section 4 we examine the contamination on the right-hand side of Eq. (3c) by the lack of simultaneity of the measurements. Any version of Eq. (3) is the well-known quasi-geostrophic potential vorticity equation (see Gill, 1982; Hoskins *et al.,* 1985) but, for this equation to be solved, boundary conditions are needed. Atmospheric

inversion problems usually lack the restriction of lateral boundary conditions and use P_V sheets at the top and bottom to simulate variable densities or temperatures at those boundaries (e.g.: Hoskins *et al.,* 1985). A well-known property of elliptic equations like (3c) is its association with a variational principle; the one pertaining to this case (Dikiy, 1969) is:

$$I(\tilde{u},\, \tilde{v},\, \tilde{\rho}) = \int\int\int \left[\rho_o \frac{(u-\tilde{u})^2 + (v-\tilde{v})^2}{2} + \frac{g^2(\rho-\tilde{\rho})^2}{2\rho_o N^2} \right] dxdydz, \tag{5}$$

with (4) required to hold. The possible observation of vertical velocity is irrelevant since the geostrophic flow (f-plane dynamics) is horizontal. The study of Dikiy (1969) includes the effects of compressibility but considers only regular boundaries. The solution given in the Appendix shows explicitly why the extremum is a minimum and how the natural boundary conditions arise for irregular domains. These boundary conditions are the remaining pieces needed to extract the geostrophic contribution from the measurements.

The variational problem of finding an extremum of I under the constraints of system (4) can be translated into a variational problem on the single field $\tilde{p}$, without need for Lagrange multipliers since the constraints (system (4)) can be included directly into the functional without further complications, giving instead of Eq. (5):

$$I(\tilde{p}) = \int\int\int \left[\rho_o \frac{(u+\tilde{p}_y/(\rho_o f))^2 + (v-\tilde{p}_x/(\rho_o f))^2}{2} + \frac{g^2(\rho+\tilde{p}_z/g)^2}{2\rho_o N^2} \right] dxdydz. \tag{6}$$

The perspective should then be that the measurements provide information about the gradient of the single field $\tilde{p}$, from which the other fields of interest (related by system (4)) can be derived. The minimization of the functional is derived formally in the Appendix; the solution is the field $\tilde{p}$ that satisfies Eq. (3c) with boundary conditions

$$(\tilde{p}_x,\, \tilde{p}_y,\, \tilde{p}_z) \cdot \mathbf{n} = (-\rho_o f v,\, \rho_o f u,\, -g\rho) \cdot \mathbf{n}, \tag{7}$$

where $\mathbf{n}$ is a unit vector locally perpendicular to the boundary. Hence, for the surface, or for any portion of a horizontal boundary, the measured density coincides with the geostrophic density. Also, the measured and geostrophic horizontal velocities along any vertical boundary coincide.

We now restrict the analysis to two dimensions. Eq. (3a) can be easily interpreted by substituting the density anomaly with the vertical displacement of isopycnals, i.e.:

$$\rho = -\zeta \frac{d\bar{\rho}}{dz} = \zeta \frac{\rho_o N^2}{g}. \tag{8}$$

Hence, Eq. (3b) reads

$$\tilde{v}_x - f\tilde{\zeta}_z = v_x - f\zeta_z, \tag{9}$$

which means the geostrophic estimate retains the quasi-geostrophic potential vorticity of the observed fields, a well-known property of the geostrophic adjustment problem and of quasi-geostrophic dynamics, derived here from a principle of minimal internal wave energy. The linearized equations of motion (2) establish a balance with null potential vorticity for internal waves (Gill, 1982), which are the motions that the method intends to filter out. All the results that emerge from the conservation of potential vorticity are then in agreement with the variational principle.

Vallis (1992) provides a parallel result for the shallow water equations and it can be shown that the same results can be obtained for linearized dynamics without requiring Lagrange multipliers. Rudnick (1996) has proposed a more general formulation of the problem, with the optimization of a more ample quadratic measure with weights based on observation errors. How to choose the weights remains an open question. He applied a different ponderation for hydrography than for velocity, based on expected error variances, but any weighting that fails to conserve potential vorticity is inconsistent with linear inviscid dynamics. Unrealistic solutions with statically unstable density distributions do not occur in any significant way with our data, which suggests that observation errors must lack a signal perceptible in potential vorticity.

Some individual geostrophic density inversions in the estimates produced here are large. The maximum is 0.0967 kg m^{-3} (i.e. σ units), quite an outlier, considering it corresponds to a local $N^2 = -9.1 \times 10^{-5}$ sec^{-2}, when the mean is 2.7×10^{-5} sec^{-2}. Recall that the vertical spacing in the objective maps is 15 m; this extreme inversion occurs in a single vertical bin next to the shelf break and close to the bottom, in realization 3.b. All density inversions occur along the bottom or near the surface, and deeper than 1500 m, where N^2 is low. The largest area of statically unstable density is a patch about 100 m thick by 12 km wide, around 1600 m depth and in the middle of the channel, in case 1.1. The maximum in this patch has a local $N^2 = -5.3 \times 10^{-7}$ sec^{-2}, whereas the average $N^2 = -2.4 \times 10^{-7}$ sec^{-2}, and observations at this depth show N^2 close to 7×10^{-7} sec^{-2}. The maximum vertical extent of an inversion, about 110 m, occurs within this patch. The area of inversions in any of the six cases is less than 2.5 percent of the total, varying from 2.4 percent in case 3.a, to less than 0.2 percent in case 1.b. The objective maps of observed density show some inversions, but they are minimal, including 0.19 percent of the area with a maximum of 0.0018 kg m^{-3} in case 1.a, 0.01 percent (only two inversions) with a maximum of 0.0006 kg m^{-3} in case 2.b, and none in the rest. Any position of an inversion in the measured density map coincides with an inversion in the geostrophic density estimate. The overall rms for geostrophic density inversions is 0.0065 kg m^{-3}, and the mean stratification implies a stable density difference of 0.043 kg m^{-3}. Since the inversion's rms is then 15.1 percent of the average density difference, and they cover less than 2.5 percent of the area, we conclude that they are insignificant.

One of the strengths of this method is that it provides a direct choice for the boundary condition, one that is not straightforward in the derivation of Eq. (3c) from system (2). Any solution of Eq. (3c) with prescribed boundary conditions of the Dirichlet or Newman type

(like Eq. (7)) is unique and produces the minimum of the functional (5), constrained to the boundary condition imposed. The direct choice is that boundary condition for which such functional attains the global minimum, which coincides, as deduced in the Appendix, with the so-called 'natural boundary condition' (Courant and Hilbert, 1953).

b. Numerical implementation

All estimates of partial derivatives were done with central differences based on the objective mapping of the original fields, with values at the boundary and beyond resulting from extrapolations manufactured by the objective mapping. The determination of $N^2 = N^2(z)$ results from lateral averaging of the potential density referred to 1000 db (i.e. σ_1), thus producing a single profile per density map, and then taking vertical derivatives on this mean profile. The numerical algorithm used to solve system (5) was kept very simple, applying the grid used in the objective mapping and a standard Sequential Over-Relaxation (SOR) method, as described in Press *et al.* (1986, Chap. 19, Sec. 5). Various algorithms to impose the boundary conditions directly proved unsuccessful. The problem always being the irregular boundary. Instead, the use of the minimization itself leads to a proper solution. Since the elliptic partial differential solution equation is linear, a solution of the inhomogeneous (forced) equation with simple Dirichlet boundary conditions was built. Then, a set of Green functions, one per boundary point, was constructed out of the homogeneous equation. Any linear combination of this set added to the forced solution solves the differential equation, a suitable one being that which minimizes the functional (4), the integral being taken only in the area of interest, the hydrographic section. This technique is very similar to the Capacitance Matrix method discussed by Parés-Sierra and Vallis (1989) and Özsoy *et al.* (1992), but the minimization with respect to the coefficients used in the expansion is what distinguishes our method from the standard Capacitance Matrix technique.

4. Error estimation

The sources of errors in this calculation are several. In classical geostrophic estimates (Johns *et al.,* 1989) the predominant errors come from (1) the density profile measurement (more precisely in the dynamic height anomaly) (2) the station positioning (ship drift), and (3) the reference velocity. For example, in the data of Johns *et al.* (1989) in the Gulf Stream the second source dominates, whereas for the measurements of Beal and Bryden (1999) in the Agulhas Current the third term is the largest. In both examples the barotropic flow was determined independently and tidal flows were small, so the problem of the reference velocity was minimized. In our nonclassical geostrophic estimate the sources of errors include the first two above, but the third must be modified as (3) measurement errors of the entire velocity profile, so that sources of error are any factors that modify the actual potential vorticity. In addition, we must also consider (4) errors associated with the boundary conditions, since the velocity and density fields obtained from the optimization are influenced by the measured values at the boundary.

An extensive error analysis for this method is beyond the scope of this study, but the largest source of error for this data set can be anticipated to be the tides. As stated in the Appendix, this geostrophic estimate duplicates the measured transport partly because of the boundary conditions used in the inversion. Tides are mostly barotropic and lack a potential vorticity signature, but can influence the estimate due to the nonsimultaneity of the observations and by contaminating the observed boundary values required for inversion. The tidal currents in the Yucatan Channel are dominated by diurnal components. Maul *et al.* (1985) measured diurnal tidal currents with amplitudes from 3 to 4 cm sec^{-1} at a distance 145 m above the sill. Durham (1972) reported diurnal components with amplitudes from 4 to 7 cm sec^{-1} in the 400 m near the surface at the same location, and calculated transports through the channel of 12.6 and 11.3 Sv for the K_1 and O_1 tidal components, with an rms inaccuracy of 4 Sv each. This is consistent with a bulk estimate based on a mean amplitude of 6 and 5 cm sec^{-1} for each component, an error of 2 cm sec^{-1}, and a cross-sectional area of 230 km^2. For this cross-section, a mean velocity of 1 cm sec^{-1} results in nearly 2 Sv of transport.

An estimate of the error in the vertical mean of $\partial v/\partial x$ caused by the lack of simultaneity of the measurements can be derived by assuming barotropic diurnal tides with the amplitudes stated above, and the actual differences in time and position from one profile to the next. Without a specific time origin, an rms error can be computed using Monte Carlo methods. A $\partial v/\partial x$ rms estimate due only to tides on all subsequent pairs of profiles used in this study has a mean of 0.3×10^{-5} sec^{-1}, with a maximum of 0.9×10^{-5} sec^{-1}, while the measured $\partial v/\partial x$ fluctuates from -17 to 16×10^{-5} sec^{-1}, with an rms of 0.7×10^{-5} sec^{-1}. Typical values of the barotropic (i.e. vertically integrated) $|\partial v/\partial x|$ on the high-shear regions of the mean velocity map are on the order of 6×10^{-5} sec^{-1}, so the lack of simultaneity introduces errors that are significant only in the portions of the flow that have little lateral shear.

If all the measurements were simultaneous the tides would only influence the geostrophic estimate via the boundary conditions since, as stated above, tides do not have a potential vorticity signal. This is because the method provides an estimate with the same transport as the measurements. The tidal transport has an rms close to 12 Sv (Durham, 1972). But, since the typical crossing takes longer than a diurnal cycle, the tidal transport averages out somehow (see Table 1 for times required for each crossing). It does, as previously explained, contaminate the velocity structure but not so much the transport, as if the observations were truly a snapshot of the fields. A 50 simulations run, with each realization having a random starting time, keeping the measured velocity and time intervals as in case 3.b, and adding diurnal barotropic tidal currents of amplitudes 6 cm sec^{-1}, and 5 cm sec^{-1}, produces an rms of 4 Sv, a maximum of 25 Sv, and a minimum of 14 Sv. The mean of 20 Sv results only from the background velocity on which the tidal noise was added (Case 3.b). Thus, tides overweight any other source of errors; the lack of simultaneity of the measurements contaminates the P_V estimate on the one hand, but reduces the tidal transport error on the other. The P_V calculations were nonetheless done using the optimally interpolated fields, so errors for the right-hand side of Eq. (3c) should be calculated using

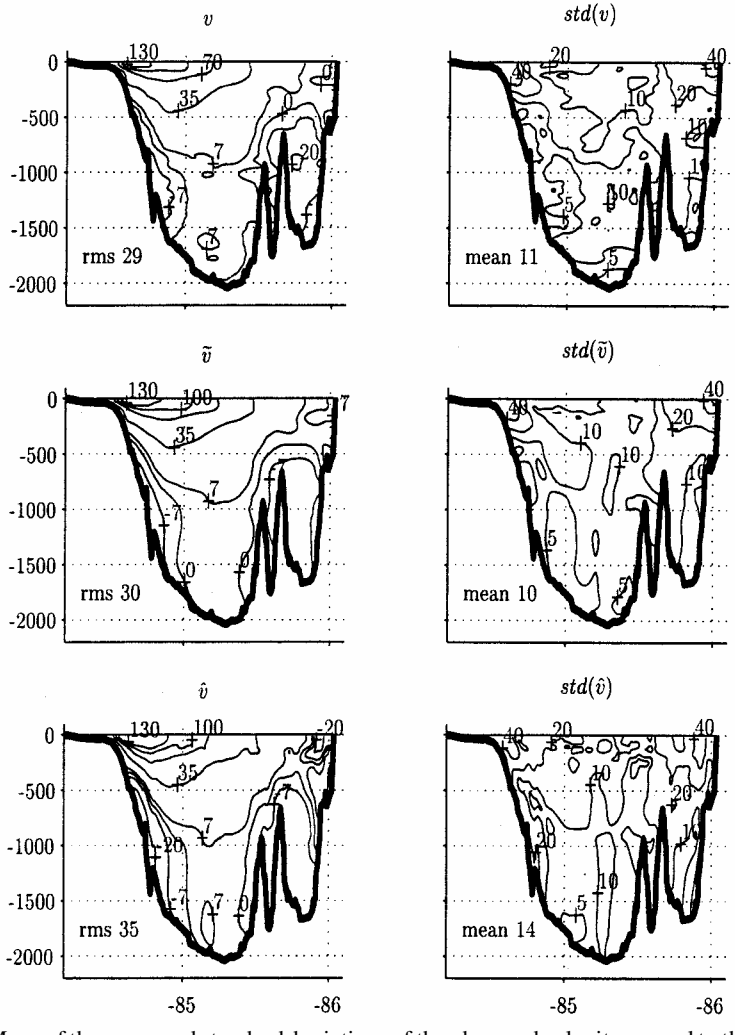

Figure 4. Maps of the mean and standard deviations of the observed velocity normal to the section v, the geostrophic velocity computed from potential vorticity inversion $\tilde{v}$ and the 'classical' geostrophic velocity $\hat{v}$ from thermal wind calculations, using the observed density field and reference LADCP measurements.

the error maps from the interpolation. On average they are 15–20% of the signal, based on our mapping assumptions and the position of the observations.

5. Results

Figure 4, panel denoted v, shows the mean of the observed velocity field normal to the section (the mean of the maps shown in Fig. 3). Panel $\tilde{v}$ shows the mean geostrophic

Table 2. Mean available kinetic and potential energies, in J m^{-2}, and the percentages of energy remaining in the anomalies. The last column is the percentage energy remaining in the anomalies using the classical geostrophic estimate.

Cruise	Kinetic	Potential	IW kinetic	IW potential	IW total	CL kinetic
1.a	34	36	1.3	1.5	2.8	16.6
1.b	44	25	1.3	1.4	2.7	11.7
2.a	43	62	1.2	0.7	1.9	5.6
2.b	33	39	1.5	1.3	2.8	11.5
3.a	52	55	1.2	1.3	2.4	10.7
3.b	50	42	1.4	1.2	2.6	13.8

velocity obtained from P_V inversion, and panel $\hat{v}$ shows the mean geostrophic velocity obtained from 'classic' geostrophy, in which the thermal wind equation is used with the observed density field and the reference velocity is determined by requiring the vertical mean of the flow normal to the section to be equal to the LADCP vertical mean, what Beal and Bryden (1999) call LADCP-referenced geostrophic velocity. The measured velocity v and the geostrophic estimate from P_V inversion are quite similar, whereas the differences between observed velocity v and the classic geostrophy $\hat{v}$ are notable, particularly in the strength of the Yucatan undercurrent on the western side of the channel, which is larger in the geostrophic field $\hat{v}$ than in the observations. The panels to the right show the corresponding standard deviations of observed and both geostrophic estimates of the normal flow from all six crossings. Standard deviation fields show large variability within the Yucatan Current and the southward Cuban Countercurrent both at the surface, and at depth, and close to the topographic features of the section in all estimates. Standard deviations in the classic geostrophic estimate are especially large compared to the observed and P_V inversion estimate (compare the bottom panel on the right with the two panels above). Table 2 provides some numbers about the 'closeness' between the geostrophic estimates and the measurements for each crossing (Fig. 2). The energy in the observed minus P_V inverted fields is less than three percent of the energy for all crossings (column 6), but the residual energy in the classical geostrophic fields is larger (column 7) and varies between 6 and 17 percent of the total energy. No potential energy exists in the residual for the classical geostrophic estimate since the observed density is used to estimate the velocity through the thermal wind balance. Table 3 shows the transports for the six realizations and their mean.

The differences between observed, geostrophy via inversion of P_V and 'classical' geostrophic fields, and the standard deviations of these differences are shown in Figure 5. The field $v - \tilde{v}$ corroborates that the difference between observed and inverted fields is small and so is their standard deviation. The largest differences reside close to the surface in the core of the Yucatan Current, an ageostrophic contribution that results probably from the size of the curvature term in the alongstream momentum balance, which indicates the current is in gradient wind balance rather than in pure geostrophic balance. The field $v - \hat{v}$ shows that the difference between observed and classical geostrophic fields is much larger

Table 3. Transports for each cruise and their mean. P_V is for the geostrophic estimate via inversion of linearized potential vorticity; CL is for the classical calculation having the same vertical average as the measured velocity. Western outflow stands for the transport into the Caribbean west of the sill, which corresponds to the undercurrent below the intense section of the Yucatan Current.

Cruise	Transport	Inflow	Outflow	Western outflow
1.a	21.7	28.0	6.3	2.0
P_V1.a		28.6	7.0	2.5
CL1.a		28.6	7.0	2.5
1.b	26.1	33.0	6.9	1.5
P_V1.b		32.5	6.3	1.1
CL1.b		34.8	8.7	2.8
2.a	31.4	38.6	7.2	2.2
P_V2.a		38.4	6.9	1.8
CL2.a		39.7	8.3	2.8
2.b	27.0	38.6	7.2	2.2
P_V2.b		32.2	5.2	1.6
CL2.b		34.5	7.5	3.0
3.a	22.3	38.0	15.7	2.7
P_V3.a		38.4	16.1	3.3
CL3.a		43.6	21.3	7.3
3.b	19.9	32.6	12.7	1.8
P_V3.b		32.8	12.9	1.9
CL3.b		36.3	16.4	4.3
Mean	24.7	33.7	9.0	2.0
P_V		33.7	9.0	2.0
CL		37.0	12.3	4.2

than the difference between observed and inverted one ($v - \tilde{v}$), which is confirmed in their standard deviations. The largest differences are again in the core of the Yucatan Current, but are about 5 times larger than those in $v - \tilde{v}$. Important differences now appear on the southerly subsurface current close to Yucatan and near the topography, as well as on the southerly surface and subsurface flows near Cuba. As will be shown below, the inversion method modifies the observed density field and is able to find a geostrophic density consistent with these southward flows. A question arises as to which of the two geostrophic velocity fields is more correct. To the extent that we lack *a priori* reason to suppose that the observed density is in geostrophic balance with the flow and that no substantial unstable density profiles are found through the inversion method, one would be inclined to favor the P_V inverted fields. Nonetheless, one should be aware that our method could still be fitting a geostrophic flow to observations in regions where the ageostrophic contributions are other than internal waves, as argued for example by Hinrichsen and Lehmann (1995). A comparison of the field $\tilde{v} - \hat{v}$ with its standard deviation on the right shows that those differences are almost as large as the ones in $v - \tilde{v}$.

Figure 6 shows the difference between the observed and geostrophic mean density fields from inversion and the standard deviation of this difference. The observed density is geostrophically 'corrected' predominantly close to the shelf break and down to 800 m depth off Yucatan, where large differences between the observed and classical geostrophic

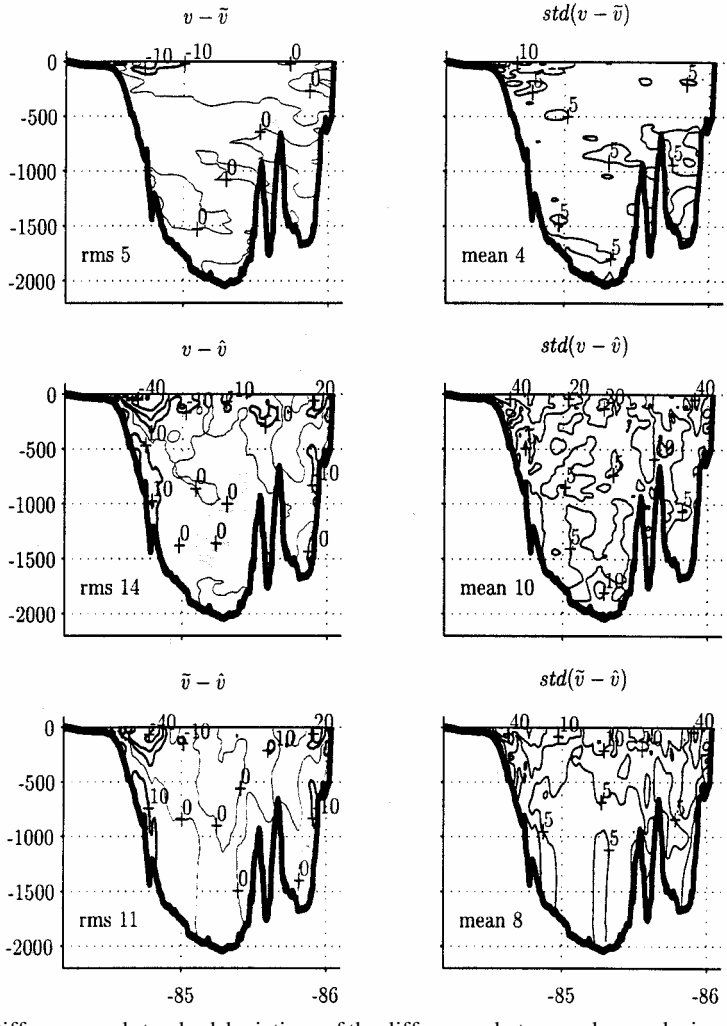

Figure 5. Difference and standard deviations of the differences between observed minus geostrophic normal velocity from P_V inversion ($v - \tilde{v}$), observed minus classic geostrophy through thermal-wind calculations ($v - \hat{v}$), and P_V inverted minus classical geostrophic estimate ($\tilde{v} - \hat{v}$). The P_V inversion yields a geostrophic velocity much closer to observations than the classical method.

velocity fields ($v - \tilde{v}$, Fig. 5) had been noted, and coincides in part with the Yucatan Undercurrent, where a southward flow hugs the Yucatan slope.

It is interesting to perform an additional calculation. The definition of $\hat{\rho}$ through

$$\hat{\rho} = \rho_r - (f\rho_o/g) \int^x v_z dx, \tag{10}$$

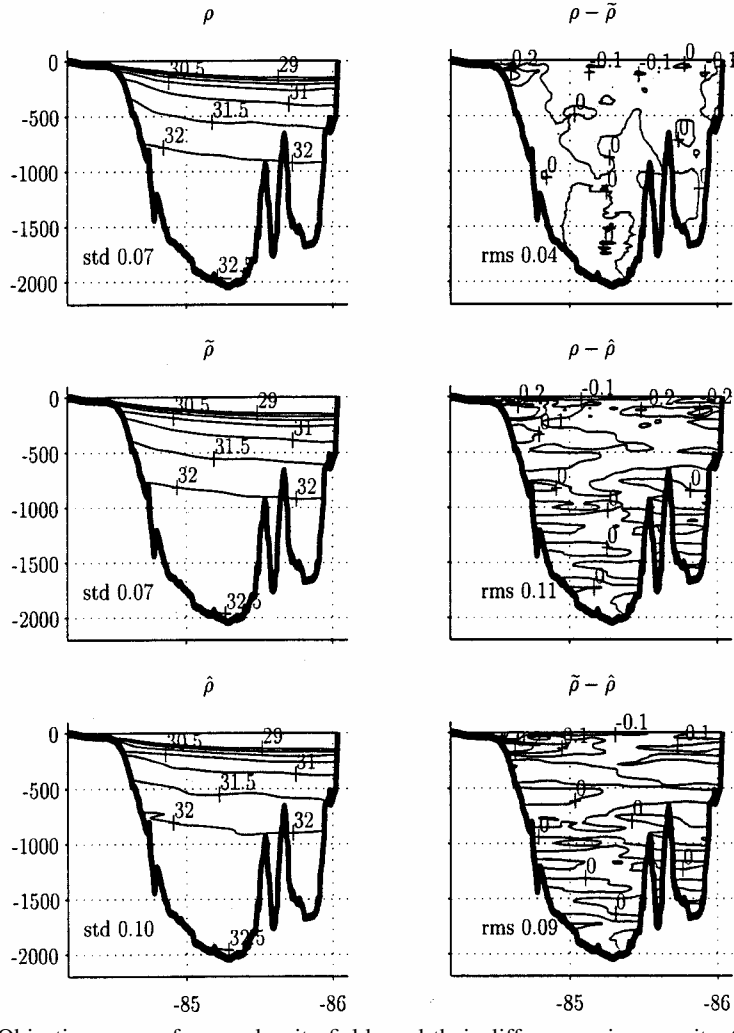

Figure 6. Objective maps of mean density fields and their differences, in σ_1 units. Observed, ρ, estimated through P_V inversion, $\tilde{\rho}$, and integration of the thermal wind equation using the observed velocity field to estimate the density $\hat{\rho}$ (Eq. 11). This 'reverse' thermal-wind produces unstable distributions possibly because of ageostrophic shears. The numerical value in the lower left corner of the mean maps is the standard deviation, and in that of the differences is the rms value.

where $\rho_r = \rho_r(z)$ is a reference density such that $\int_{side}^{side} \hat{\rho} dx = \int_{side}^{side} \rho dx$ is the symmetric use of the thermal wind equation, considering its classical use to infer geostrophic velocities. This is the direction in which observational oceanography might have evolved had acousticians dominated the field in its early stages and LADCP instruments been developed before CTD's. Figure 6 shows the observed density ρ (expressed as σ_1), the geostrophic density from P_V inversion $\tilde{\rho}$, and the density field obtained from this 'reverse'

thermal-wind relation (10), in which density is obtained from velocity observations. Again, the observed and P_V-inverted density fields are quite similar, except over the western shelf and slope off Yucatan. The density from the 'reverse' thermal-wind relation is also quite similar, despite density inversions that occur probably because near-inertial oscillations have strong velocity shears which are, of course, ageostrophic.

From a different perspective, having velocity measurements together with hydrography allows a test of the thermal wind balance. By construction, $\tilde{v} = -(g/\rho_o f)\tilde{\rho}_x$, since both sides of the equation are but a different order of differentiating $\tilde{p}$ with respect to x and z; even if the $\tilde{p}$ estimate were totally wrong, as long as it is smooth enough it will always satisfy $\partial^2\tilde{p}/\partial x\partial z = \partial^2\tilde{p}/\partial z\partial x$. Averages for all crossings of v_z/f, $\tilde{v}_z/f$ and $-(g/\rho_o f)\rho_x/f$ are 7.9, 8.9 and 9.8. The rms of $(v_z + (g/\rho_o f)\rho_x)/f$ is 23.3 and those of $(\tilde{v}_z - v_z)/f$ and $(\tilde{v}_z + (g/\rho_o f)\rho_x)/f$ are 15.4 and 15.7. The geostrophic shear $\tilde{v}_z$ falls between v_z and $-(g/\rho_o f)\rho_x$. Notice that the construction of the geostrophic estimate via P_V inversion ignores any information from the v_z or ρ_x fields (see right-hand side of Eq. 3c).

6. Discussion and conclusions

The estimation of the geostrophically balanced fields from observed hydrographic and horizontal velocity distributions is equivalent to the geostrophic adjustment of arbitrary initial fields. The conservation of quasi-geostrophic potential vorticity in the geostrophic adjustment is consistent with a process that optimizes the 'energy retained' in the static geostrophic mode. From the available energy, a minimum amount possible is radiated away within the internal wave field (at least in its linearized version); we use quotes in 'energy retained' because the space averages of $\tilde{v}^2$ and $v^2 - v'^2$ need not be the same, since the average of vv' is not necessarily null, and similarly for the density separation in its geostrophic plus anomaly contributions. The total energy is not the sum of 'geostrophic energy' and 'internal energy.' As explained by Dikiy (1969), in the geostrophic adjustment the minimum energy possible is released into the internal wave field, 'retaining' as much as possible within the geostrophic contribution.

This method is physically sound and readily applicable. One source of contamination is any factor that introduces errors in the measured potential vorticity. These errors are fed directly into this estimate, since it is the forcing of the Poisson equation to be solved (i.e. Eq. 3c), but not all measurement errors influence the measured potential vorticity. Another source of contamination comes from the boundary conditions imposed on the Poisson equation, which are influenced by ageostrophic components. For example, the addition of a constant to the measured velocity produces the same vorticity and potential vorticity, but using the natural boundary conditions implies a new geostrophic velocity with the same constant as difference from the original geostrophic velocity. Some errors which do not contribute to the potential vorticity distribution can influence the estimate through the boundary conditions.

The need to specify the boundary condition in the Poisson equation is equivalent to the traditional problem of setting the reference velocity, an unexpected and undesired result,

since this has been one of the main complications of the so-called dynamical method. One needs to realize that the geostrophic information of the measurements is in the forcing of the Poisson equation (i.e. in P_V), which resides in the derivatives of the fields. In addition, with this method the information from hydrography comes from ρ_z and not from its horizontal derivatives which, in light of the thermal wind equation, was the field traditionally obtained to integrate as an estimate of horizontal velocities. All the diagnostic requirements of the thermal wind equation are completely fulfilled with the existence of the geostrophic pressure and that is the function this method aims to quantify.

Our measurements in the Yucatan Channel show three well-known characteristics of the flow: the Yucatan Current, its Undercurrent, and the Cuban Countercurrent. A feature unreported previously is the mean southerly flow above the abrupt topography on the eastern side of the channel between 500 and 1500 m depth. This current transports on the order of 2 Sv and might well be the recirculation of waters of the same depths that enter the gulf farther to the west as the deep expression of the Loop Current but, unable to flow out through the Florida Straits, continue in an anticyclonic circulation and return to the Caribbean Sea.

Acknowledgments. This research was supported by CICESE, the Consejo Nacional de Ciencia y Tecnología of Mexico, and the Inter-Americas Institute for Global Change, through project Canek. We acknowledge the Universidad Nacional Autónoma de México (UNAM) for its support with shiptime and the crew of the R/V *Justo Sierra,* Captain Leobardo Ríos commanding, for their participation in our operations. Ignacio González, Ryan Smith and Joaquín García were fundamental in the data processing. J. O. wishes to acknowledge financial support from CONACyT for a sabbatical stay at RSMAS, Miami, made possible and enjoyable by the hospitality of Chris Mooers and all of OPEL's personnel. We thank the Instituto de Oceanología de Cuba for their collaboration in the program and the technical staff at CICESE for making our cruises a success.

APPENDIX

Estimate of the internal wave field of minimum energy, constrained to a given snapshot of the horizontal velocity and density distributions

We derive the requirements on the field $\tilde{p}$ for which the functional defined in Eqs (5) and (6) attains an extremum, which is shown to be unique and a minimum. To save space, consider the notation $a_1 = \rho_o fv$, $a_2 = -\rho_o fu$, $a_3 = -gf\rho/N$, $\tilde{p} = P$ and $I' = 2\rho_o fI$, and the change of variables $x = x'$, $y = y'$ and $dz = fN^{-1}dz'$ (i.e. $z' = f^{-1}\int N dz$). Then, equivalent to Eq. (4), we have

$$I'(P) = \int N^{-1}|\mathbf{a} - \nabla' P|^2 dV', \tag{A.1}$$

where the integral is over the volume in transformed space ($dV' = dx'dy'dz'$), $\mathbf{a} = (a_1, a_2, a_3)$, and the operator $\nabla' = (\partial/\partial x', \partial/\partial y', \partial/\partial z')$. This is a problem in potential theory whose aim is to find a weighted (by $N^{-1} > 0$) least-square potential function (P) from an approximation of its gradient ($\mathbf{a}$). A seemingly unrealistic limitation of this formulation is

the requirement of a positive definite N, but the distribution of N used can be, holding this restriction, as close to the realistic profiles as desired. A straightforward evaluation of its variation (i.e. $\Delta I'(P, \delta P) = I'(P + \delta P) - I'(P)$) gives

$$\Delta I' = -2 \int N^{-1} \nabla' \delta P \cdot (\mathbf{a} - \nabla' P) dV' + \int N^{-1} |\nabla' \delta P|^2 dV', \tag{A.2}$$

from which is clear that if the first integral on the r.h.s. is null, then $\Delta I' > 0$ for all δP which are not a uniform constant. The addition of a constant to a potential function plays no role.

The use of the mathematical identity $\int \mathbf{B} \cdot d\boldsymbol{\sigma}' = \int \nabla' \cdot \mathbf{B} dV'$, where $\boldsymbol{\sigma}'$ is the surface vector locally perpendicular to the boundary and pointing outward in the transformed coordinates, with $\mathbf{B} = N^{-1} \delta P(\mathbf{a} - \nabla' P)$, enables to write the first integral on the r.h.s. of Eq. (A.2) as

$$\int N^{-1} \nabla' \delta P \cdot (\mathbf{a} - \nabla' P) dV' = \int N^{-1} \delta P (\mathbf{a} - \nabla' P) \cdot d\boldsymbol{\sigma}' - \int \delta P \nabla' \cdot [N^{-1}(\mathbf{a} - \nabla' P)] dV', \tag{A.3}$$

which is an 'integration by parts' in 3-D. Thus if

$$\nabla' \cdot [N^{-1}(\mathbf{a} - \nabla' P)] = 0, \tag{A.4a}$$

and

$$(\mathbf{a} - \nabla' P) \cdot \mathbf{n} = 0, \tag{A.4b}$$

where $\mathbf{n}$ is a vector locally perpendicular to the boundary, are fulfilled then, regardless of δP, $\Delta I'$ cannot be negative and is therefore a minimum of I'. Eq. (A.4b) is known as the 'Natural Boundary Conditions' of the Poisson equation (A.4a) (see for example Courant and Hilbert, 1953). This derivation shows that the 'Natural Boundary Conditions' are required for the global minima of the functional (A.1). System (A.4) expressed in the original variables are Eqs. (3c) and (7).

For a constant, uniform N this formulation is part of the Helmoltz Theorem about the decomposition of a vector field as the gradient of a scalar potential field plus the rotational of a vector field. P in system A.4 is the scalar potential part of $\mathbf{a}$. The conservation of linearized potential vorticity is the fulfillment of the conditions $\nabla \cdot \nabla P = \nabla \cdot \mathbf{a}$ in the least-square solution of $\nabla P = \mathbf{a} + \mathbf{a}'$, where $\mathbf{a}$ is given and the anomaly $\mathbf{a}'$ is minimized.

It is worth pointing out that, given the solution (i.e. the function $P = P(x', y', z')$ that satisfies A.4), $\int N^{-1} \nabla' \delta P \cdot (\mathbf{a} - \nabla' P) dV'$ equals zero for any $\delta P = \delta P(x', y', z')$, therefore by properly choosing δP it follows, in the reduction of Eq. (5) to 2-D, that

$$\int \int (v - \tilde{v}) dx dz = 0, \tag{A.5}$$

and

$$\int\int (\rho - \tilde{\rho}) dxdz = 0. \tag{A.6}$$

The mean velocity and net transport of the measurements coincide with the mean velocity and net transport of the geostrophic estimate, and the mean observed density equals the mean geostrophic density.

REFERENCES

Beal, L. M. and H. L. Bryden. 1999. The velocity and vorticity structure of the Agulhas Current at 32°S. J. Geophys. Res., *104,* 5151–5176.

Brooks, I. H. and P. P. Niiler. 1977. Energetics of the Florida Current. J. Mar. Res., *35,* 163–191.

Carrillo, F., J. L. Ochoa, J. Candela, O. Ramírez and I. González. 2000. Corrientes de marea en el canal de Yucatán. 5° Congreso de Ciencias del Mar, Marcuba 2000, Programa Científico, La Habana, 91.

Cokelet, E. D., M. L. Schall and D. M. Dougherty. 1996. ADCP-referenced geostrophic circulation in the Bering Sea Basin. J. Phys. Oceanogr., *26,* 1113–1128.

Courant, R. and D. Hilbert. 1953. Methods of Mathematical Physics, Wiley-Interscience, New York, NY, 561 pp.

Chereskin, T. K. and M. Trunnell. 1996. Correlation scales, objective mapping and absolute flow in the California Current. J. Geophys. Res., *101,* 22619–22629.

Daley, R. 1991. Atmospheric Data Analysis. Cambridge University Press, NY. 457 pp.

Dikiy, L. A. 1969. A variational principle in the theory of meteorological-field adaptation. Izv. Atmos. Ocean. Phys., *5,* 188–191.

Durham, D. L. 1972. Estimates of Diurnal Tidal Volume Transports Through the Yucatan Channel. Ph.D. Dissertation, Texas A&M University, 173 pp.

Emilsson, I. 1971. Note on the countercurrent in the Yucatan Channel and the western Cayman Sea. Geofís. Int., *11,* 139–149.

Fischer, J. and M. Visbeck. 1993. Deep velocity profiling with self-contained ADCPs. J. Atmos. Ocean. Technol., *10,* 764–773.

Fratantoni, D. M. and W. E. Johns. 1996. A deep-towed ADCP-CTD instrument package development for abyssal overflow measurements in the northeastern Caribbean Sea. J. Atmos. Ocean. Technol., *13,* 680–687.

Gallegos, A., I. Victoria, J. Zavala, M. Fernández and I. Penié. 1998. Hidrología de los estrechos del Mar Caribe noroccidental. Rev. Invest. Mar., *19,* 1–37.

Gill, A. E. 1982. Atmosphere-Ocean Dynamics, Academic Press, London, 662 pp.

Gordon, A. E. 1967. Circulation of the Caribbean Sea. J. Geophys. Res., *72,* 6207–6223.

Hansen, D. V. and R. L. Molinari. 1979. Deep currents in the Yucatan Strait. J. Geophys. Res., *84,* 359–362.

Hinrichsen, H. H. and A. Lehmann. 1995. A comparison of geostrophic velocities and profiling ADCP measurements in the Iberian basin. J. Atmos. Ocean. Technol., *12,* 901–914.

Hoskins, B. J., I. Draghici and H. C. Davis. 1978. A new look at the omega-equation. Quart. J. Roy. Meteor. Soc., *104,* 31–38.

Hoskins, B. J., M. E. McIntyre and A. W. Robertson. 1985. On the use and significance of isentropic potential vorticity maps. Quart. J. Roy. Meteor. Soc., *111,* 872–946.

Johns, E., D. R. Watts and H. T. Rossby. 1989. A test of geostrophy in the Gulf Stream. J. Geophys. Res., *94,* 3211–3222.

Lee, T. N. and D. A. Mayer. 1977. Low frequency current variability and spinoff eddies on the shelf off southeast Florida. J. Mar. Res., *35,* 193–220.

Maul, G. A., D. A. Mayer and S. R. Baig. 1985. Comparisons between a continuous 3-year current-meter observation at the sill of the Yucatan Strait, satellite measurements of Gulf Loop Current area, and regional sea level. J. Geophys. Res., *90,* 9089–9096.

Merino, M. 1997. Upwelling on the Yucatan shelf: hydrographic evidence. J. Mar. Syst., *13,* 101–121.

Molinari, R. L. 1976. The formation of the Yucatan Current based on observations of summer 1971. J. Phys. Oceanogr., *6,* 596–602.

Özsoy, E., C. J. Lozano and A. Robinson. 1992. A consistent baroclinic quasigeostrophic ocean model in multiply connected ocean domains. Math. Comp. Sim., *34,* 51–79.

Parés-Sierra, A. and G. K. Vallis. 1989. A fast semi-direct method for the numerical solution of non-separable elliptic equations in irregular domains. J. Comp. Phys., *82,* 398–412.

Pillsbury, J. E. 1890. The Gulf Stream—A description of the methods employed in the investigation, and the results of the research, USCC-Geodetic Survey, Silver Spring, Md, 461–620.

Pinot, J. M., J. Tintoré and D. P. Wang. 1996. A study of the omega equation for diagnosing vertical motions at ocean fronts. J. Mar. Res., *54,* 239–259.

Pollard, R. T. and L. A. Regier. 1992. Vorticity and vertical circulation at an ocean front. J. Phys. Oceanogr., *22,* 609–625.

Press, W. H., S. A. Teukolsky, W. T. Vetterling and B. P. Flannery. 1986. World Wide Web sample pages from Numerical Recipes in Fortran; the art of scientific computing. Cambridge University Press. http://www.nr.com/nronline_switcher.html. 1986–1992.

Reid, J. L. 1994. On the total geostrophic circulation of the North Atlantic Ocean: Flow patterns, tracers, and transports. Prog. Oceanogr., *33,* 1–92.

Ripa, P. M. 1997. Ondas y dinámica oceánica, *in* Contribuciones a la Oceanografía Física en México, M. F. Lavín, ed. Monografía No. 3, Unión Geofísica Mexicana, 47–74.

Roemmich, D. 1983. Optimal estimation of hydrographic station data and derived fields. J. Phys. Oceanogr., *13,* 1544–1549.

Rudnick, D. L. 1996. Intensive surveys of the Azores Front 2. Inferring the geostrophic and vertical velocity fields. J. Geophys. Res., *101,* 16291–16303.

Saunders, P. M. 1992. Combining hydrographic and shipborne ADCP measurements. Deep-Sea Res., *39,* 1417–1427.

Shearman, R. K., J. A. Barth and P. M. Kosro. 1999. Diagnosis of the three-dimensional circulation associated with mesoscale motion in the California Current. J. Phys. Oceanogr., *29,* 651–670.

Schlitz, R. J. 1973. Net Total Transport and Net Transport by Water Mass Categories for Yucatan Channel, Based on Data for April 1970. Ph. D. Dissertation, Texas A&M University, 107 pp.

Sturges, W. and J. C. Evans. 1983. On the variability of the Loop Current in the Gulf of Mexico. J. Mar. Res., *41,* 639–653.

Sukhovey, V. F., G. K. Korotaev and N. B. Shapiro. 1980. Hydrology of the Caribbean Sea and Gulf of Mexico. Leningrad, Geometeoizdat (in Russian), 180 pp.

Vallis, G. K. 1992. Mechanisms and parameterizations of geostrophic adjustment and a variational approach to balanced flows. J. Atmos. Sci., *49,* 1144–1160.

Wilson, W. D. 1994. Deep ocean current profiling with a broad-band acoustic Doppler current profiler. Oceans'94, Proceedings, IEEE/MTS.

Wilson, W. D. and W. E. Johns. 1997. Velocity structure and transport in the Windward Islands Passages. Deep-Sea Res., *44,* 487–520.

Wilson, W. D. and A. Leetmaa. 1988. Acoustic Doppler current profiling in the Equatorial Eastern Pacific in 1984. J. Geophys. Res., *93,* 13947–13966.

Received: *9 September, 1998;* revised: *16 August, 2001.*